JOURNAL OF MATERIALS SCIENCE 33 (1998) 4677–4685

Nanoindentation technique for measuring residual stress field around a laser-induced crack in fused silica

F. DAHMANI*, J. C. LAMBROPOULOS*, A. W. SCHMID, S. J. BURNS*, C. PRATT*
*Laboratory for Laser Energetics and *Department of Mechanical Engineering, University of Rochester, 250 East River Road, Rochester, NY 14623-1299, USA*
E-mail: fdah@lle.rochester.edu

A nanometre scale indentation technique using microprobe indentations to measure residual stresses at selected positions near u.v.-laser-induced cracks in fused silica is presented. The approach is based on the observation that the nanoindentations' penetration depths are affected by the residual stress field emanating from the laser-induced crack. A simple theoretical model based on the change of the nanoindentation penetration depth as well as the change in Young's modulus and hardness of the material is derived. The results show good agreement with the inclusion model [15] suggesting that the residual stress field around a laser-induced crack in fused silica is of shear nature. An exploratory test made on an unstressed sample (free of a laser-induced crack), yielding values for Young's modulus and hardness in accordance with handbook values, shows the high accuracy of this nanoindentation diagnostic.

1. Introduction

Because of its excellent transmissive properties over a wide wavelength range, including the u.v., fused silica is a preferred material for many high-fluence laser applications; it is widely used for large spatial filter lenses that also serve as vacuum windows for high-fluence lasers such as Nova and Beamlet [1–3]. With almost no exception, however, the useful output of these high-power lasers is limited by laser-induced damage to optical components. This situation has existed throughout the three-decade history of lasers, and will exist for the foreseeable future. Therefore, it is important to have good knowledge of, among other things, the opto-mechanical properties of the laser materials that may get, or have already been damaged (i.e. index of refraction around the damage zone and the fracture strength).

When a low-fluence laser beam passes through a transparent substrate, little or no material response may be observed. When the fluence of the beam is increased sufficiently, however, a whole range of reversible interactions may be activated: strain [4], distortion [4, 5], temperature rise [6], non-linear transmittance [7], electro-optic effects [8], second-harmonic generation [9], optical parametric oscillation [10], or self-focusing [11]. When the beam fluence is increased further, these phenomena give way to irreversible changes in the material: cracking, pitting, melting, and vaporization. Measured surface-damage (damage is defined to be any visible permanent modification to the probed surface observable as scatter sites under a dark-field microscope) thresholds in air at near-normal incidence are higher for the entrance than for the exit surface (the "threshold value" is assigned here midway between the lowest fluence that produces damage and the highest that does not). The optical breakdown fluences are in fact equal for both surfaces, once reflections and phase shifts of the optical fields at each interface are taken into account. For a perfect sample with refractive index n, the ratio of exit to entrance damage thresholds is $F_{\text{exit/th}}/F_{\text{entrance/th}} = (n+1)^2/4n^2$ [12]. A standing wave is formed with a maximum constructive energy density at $\lambda_L/2$ (where λ_L is the laser wavelength) in front of the surface. This usually results in the formation of a plasma at this point. In the case of the entrance surface, this plasma occurs in air, shielding the sample by absorption of the incident fluence. At the exit surface, the intensity enhancement occurs inside the material, thus increasing the initiation probability damage; therefore, this paper focuses primarily on exit-surface damage.

Laser-induced cracks (LIC) are widely used to investigate fracture processes and fatigue life in fused-silica [3, 13] Strength analysis of most glass materials is based on a somewhat idealized picture of Griffith flaws [14]. Detailed investigations of specific flaw-generation processes in fused-silica material suggest, however, that, in general, this picture requires modification [15]. When the fluence of an input laser pulse is above a certain, sample-specific threshold value and under subsequent cyclic laser shots, the damage process causes microscopic volume changes, giving rise to thermomechanical stresses. These stresses, resulting from the expansion mismatch between the crack and the rest of the matrix, induce birefringence in the fused-silica system. In such a case, the residual field can significantly modify the stability of subsequent crack expansion in an

applied stress field and thus affect the strength characteristics. In another paper [16], this residual stress field was deduced by measuring the optical birefringence surrounding a laser-induced crack. In that work, a variable Soleil compensator was used, and the stress field, viewed between crossed polars, was measured and explained in terms of a theoretical model developed for the purpose. Reasonable agreement with the data of others [17] was also ascertained, yet the Soleil-compensator technique is time consuming and does not allow high-spatial-resolution measurements.

Looking to overcome this limitation, we report in the present work a new experimental technique for measuring the residual stress field near a laser-induced crack. This technique uses nanoindentations as submicron-resolution probes for the residual stress at specific positions near a laser-induced crack. These measurements are made possible by a new class of diagnostic instruments that continuously measure the load and displacement as a controllable indentation progresses [18–20]. Based on load–displacement data, this technique yields various engineering parameter values [for example, Young's modulus (E) and hardness (H)] from the subsurface region without affecting the material under test (because of the very small indentations made), permitting further experimental investigations, including fracture-strength measurements under four-point bending [16].

2. Experimental description

2.1. Specimen preparation and laser-induced crack growth

Polished fused silica (Corning 7940 UV-grade A) bars of nominal size $64 \times 13.6 \times 4.6$ mm were used. All samples were simultaneously polished on the same pitch lap. The r.m.s. roughness of the final surface, measured by a Zygo interferometer, was typically < 0.6 nm. Before laser irradiation, samples were cleaned by the standard drag–wipe technique used to clean sensitive optical components. A total of three samples was used in this experiment.

The laser beam irradiating the samples was generated by a pulsed, high-power Nd:glass laser unit. Pulses (500 ps) were focused onto the sample surface by a fused-silica lens (focal length $f = 2$ m) giving a focal spot of $1.2\,(\pm 0.3)$-mm diameter (at $1/e^2$) at $\lambda_L = 351$ nm. The samples were mounted on an x–y translation stage and moved back and forth between the laser beam path and a $110\times$ dark-field microscope to allow automatic sample inspection after each shot. Fresh sites were irradiated on each shot, with the fluence increased stepwise until damage on the sample exit surface was observed. The threshold fluence for damage was determined by taking the average over fluence values falling into the range between the highest non-damaging fluence level and the lowest damaging fluence level [21]. Once the inducing-damage-threshold fluence for the exit surface, $F_{\text{exit/th}}$, was thus measured, all the damaged specimens were irradiated at the same laser fluence F_L (with $F_L > F_{\text{exit/th}}$), with different numbers of laser shots, N, to allow for crack propagation.

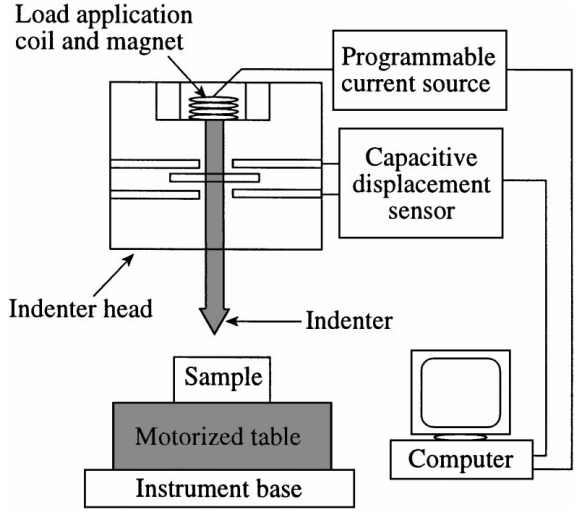

Figure 1 Schematic representation of the Nano Indenter® II system used to perform the indentation experiments. The coil and magnet move the indenter. Motion of the specimen in the x–y–z direction is accomplished by the motorized table. For the sake of clarity, the microscope and electronic camera are not shown.

2.2. Indentation procedure

All fused-silica, laser-precracked specimens were indented using a Nano Indenter® II system [22] at the Center for Optics Manufacturing (University of Rochester). A schematic of the set up is shown in Fig. 1. The instrument consists of three major components: (1) a Berkovich indenter – a three-sided diamond pyramid with an area-to-depth function that is the same as that of a Vickers' indenter; (2) an optical microscope equipped with a TV camera to image the specimen remotely (the microscope-TV camera set has a maximum magnification of approximately $1500\times$); (3) an x–y–z precision table that transports the specimen between the microscope and the indenter, with a spatial resolution in the x–y plane of ± 0.4 μm. Unlike conventional hardness testers [23–31], this indenter does not require determining *optically* the area of an indent in order to derive material hardness. Instead, the height position of the indenter relative to the specimen surface is constantly monitored, thus allowing the depth of an indent to be determined. The area of the indent is then *calculated* from prior knowledge of the diamond indenter tip geometry. The system has manufacturer-specified, theoretical load and displacement resolutions of ± 0.1 μN and ± 0.04 nm (experimentally limited by the noise in the DVM), respectively.

All the indents performed consisted of several segments as reported in Table I: (1) The first is always an "Approach Segment (A)," which incorporates instructions that allow the computer to locate the relative positions of the indenter and the sample surface in the vertical direction, i.e., the "zero" point of the displacement and load data. (2) A "Load Segment (LL)": the indent is made under load control at a constant loading rate of 35 mN s^{-1} with the load increasing until a total load of 350 mN is applied to the indenter. (3) A short "Hold Segment (H)" is then inserted at the end of the load segment to allow the system to come to equilibrium before initiating the next segment. (4) An "Unload Segment (UL)" is load controlled with an unloading rate equal

TABLE I Typical indent experiment segments performed on fused-silica samples

1	A
2	LL, 35000Rat, 350000For
3	H, 0Rat, 2Log, 50Poi
4	UL, 100%Ra, 90%Un
5	H, Ra, 2Log, 50Poi
6	UL, 100%Ra, 100%Un

Segment 1 is the Approach Segment (A). Segment 2 is a load-controlled Load Segment (LL); the indent is made at a constant loading rate of 35 000 μN s^{-1} until a total load of 350 000 μN is applied to the indenter. Segment 3 is a Hold Segment (H); two points (i.e. a load–displacement pair) are logged every second until a total of 50 points has been accumulated. The purpose of including this segment is to provide data for calculating the thermal drift of the samples during the indenting process. The load is reduced in Segment 4 [Unload Segment (UL)] at a rate equal to 100% of the loading rate until 90% of the total load used in Segment 2 is removed. Segment 5 is the second Hold Segment. Segment 6 is the second and final Unload Segment. The unloading rate is again 100% of the load at the end of Segment 2, and 100% of the load is removed.

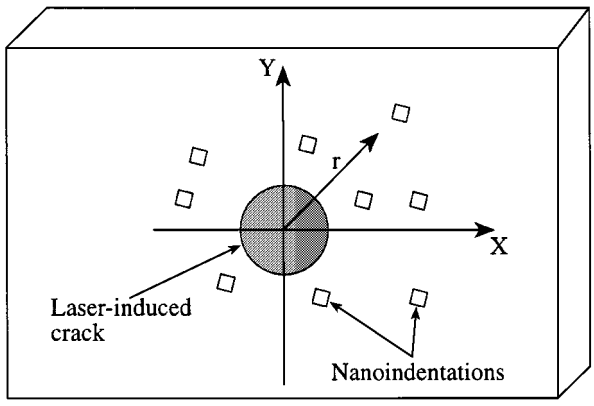

Figure 2 Schematic illustration showing the nanoindentation experiments. The nanoindentations are made at different positions relative to the center of the laser-induced crack.

to 100% of the loading rate at the end of the previous hold segment. The unloading continues until 90% of the load segment has been removed from the indenter (5) and (6). The experiments end with a second Hold Segment and a final *Unload Segment*, in which 100% (the default value) of the load is removed.

As already stated, when the fluence of the input laser pulse is above the threshold value and under a subsequent number of laser shots, macroscopic volume changes (crack initiation and crack propagation) take place in the material generating mechanical and/or thermo-mechanical stresses. These stresses create a residual stress field around the crack. If a nanoindentation is now placed near the laser-induced crack (Fig. 2), the penetration depth of this nanoindentation will be affected by both the residual stress field emanating from the laser-induced crack and any stress field that may have existed prior to crack formation, for instance, one attributable to surface polishing [32–37]. At a constant indent load, the penetration depth of each nanoindentation will depend on the distance of the particular indent from the center of the laser-induced crack. By measuring these penetration-depth values, and comparing them with those from nanoindentations made at the same load but without the effect of additional stress (indentations made on a sample free of laser-induced cracks), the residual stress field around the laser-induced crack can be calculated using the simple analysis presented in Section. 3.1. One of the advantages of using nanoindentations is that they do not alter the stress field created by the laser-induced crack because of their very small sizes. Their effect on the stress field of the laser-induced crack can be ignored. Also, the fracture strength measurements on such samples under bending test are not affected.

3. Results and discussion

3.1. Theoretical analysis

Nanoindentations performed in this study are envisioned as shown in Fig. 3. At any time during loading, the total displacement or depth d is written as [38]

$$d = d_c + d_s \tag{1}$$

where d_c is the contact depth along which contact is made and d_s is the displacement of the surface at the perimeter of the contact. At maximum loading, the load and displacement are $P = P_{max}$ and $d = d_{max}$, respectively, and the radius of the contact circle is b. Upon unloading, the elastic displacements are recovered, and when the indenter is fully withdrawn, $P = 0$, the final equilibrium depth is d_f. Fig. 4 shows a typical load-displacement curve obtained for an unstressed fused-silica sample (free of any laser-induced crack). The two important parameters are the maximum load (P_{max}) and the depth at $P = 0$ (d_f).

To calculate the residual stress field around a laser-induced crack (LIC), we first consider a microindentation made in an unstressed sample. According to Anstis *et al.* [27, 39], the mode I stress intensity factor – assuming that at this very low load stage the crack size, c, of the indent is of the same order as the penetration depth – takes on the form

$$K = \frac{\chi_r P_{max}}{d_{0f}^{3/2}} = K_C \tag{2}$$

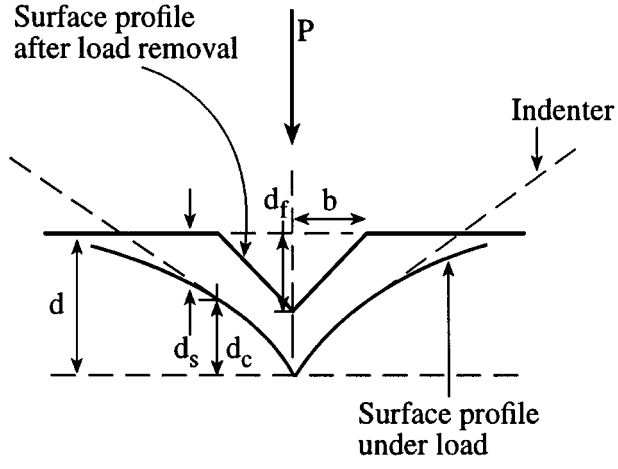

Figure 3 Cross-sectional schematic of indentation geometry used in this experiment. For meaning of symbols refer to the text.

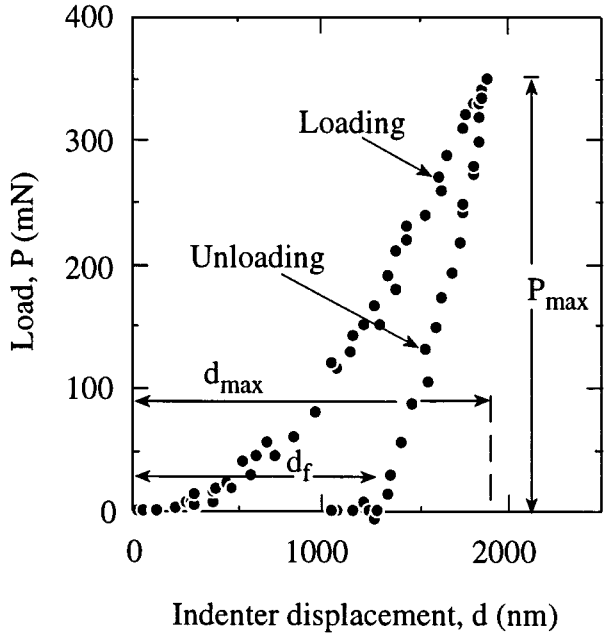

Figure 4 Load versus indenter displacement for the peak load of 350-mN experiment performed on an unstressed fused-silica sample. The final penetration depth d_{0f} is 1.322 μm.

where K_C is a critical value identifiable with material "toughness"; P_{max} is the indentation maximum load, d_{0f}, replacing the crack size, c, is the final equilibrium indentation depth; and χ_r is a dimensionless number associated with the contact residual stress field [40] and related to the elastic modulus/hardness ratio E/H. It follows from Ref. [39] that χ_r can be written as

$$\chi_r = B\left(\frac{E}{H}\right)^{1/2} \tag{3}$$

where B represents here a constant for Berkovich-tip-produced radial cracks. The net stress intensity factor for an unstressed material is therefore

$$K = B\left(\frac{E_0}{H_0}\right)^{1/2}\frac{P_{max}}{d_{0f}^{3/2}} = K_C \tag{4}$$

where E_0 and H_0 correspond to Young's modulus and hardness of the bulk (unstressed) fused-silica material, respectively.

Now, in the presence of a laser-induced crack (stressed samples), and because of its residual stress field, the final microindentation depth becomes d_{f^*}. Assuming again crack growth under equilibrium conditions $K = K_C$, Equation 4 becomes [27]

$$K = K_C = B\left(\frac{E_*}{H_*}\right)^{1/2}\frac{P_{max}}{d_{f^*}^{3/2}} + \sigma_r Y(\pi d_{f^*})^{1/2} \tag{5}$$

where Y is a dimensionless constant related to the indentation geometry (we assume $Y = 1$ in our calculations), and σ_r is the residual stress of the LIC. E^* and H^* are the values of Young's modulus and hardness of fused silica, respectively, in the presence of a laser-induced crack at a given indent position. Substituting ($B \times P_{max}$) from Equation 4 and then rearranging Equation 5, we obtain for the residual stress field emanating from the LIC

$$\sigma_r = \frac{K_C}{(\pi d_{f^*})^{1/2}}\left[1 - \left(\frac{E_*}{E_0}\,\frac{H_0}{H_*}\right)^{1/2}\left(\frac{d_{0f}}{d_{f^*}}\right)^{3/2}\right] \tag{6}$$

Note the change in σ_r as the final depth of the microindentation varies from sample site to sample site. We point out the usefulness of Equation 6 in deriving values for the residual stress field at any point around the laser-induced crack, only from the measurement of the changes of the microindentation final depth, Young's modulus, and material hardness at the position of the indentation.

3.2. Exit-surface damage threshold and crack propagation

The damage is defined to be any visible permanent modification to the exit-surface observable as one or more scatter sites under the dark-field microscope. The smallest observable damage spots are approximately 1 μm in diameter at a measured damage-threshold value of $F_L = F_{exit/th} = 10$ J cm^{-2}. This localized site or set of sites form the origination point for subsequent crack formation and growth.

To study the dependence of crack growth on the number of laser shots N three laser-predamaged fused-silica samples were irradiated at above-threshold and constant laser fluence $F_L = 2.2 \times F_{exit/th}$. By increasing the number of laser shots, the crack initiates and propagates from the specimen's exit-surface toward the entrance surface. The three samples were exposed to different numbers of laser shots at $F_L = 2.2 \times F_{exit/th}$.

Fig. 5 shows a series of typical laser-induced crack patterns in fused silica irradiated at laser fluence of $F_L = 2.2 \times F_{exit/th}$ with different numbers of laser shots. One can clearly observe that the crack surface length $2c$ saturates at a value of the order of the laser focus diameter [15], while the crack depth a increases, without apparent saturation, with the number of laser shots. Reference [16] shows that the crack depth scales with the number of laser shots as $N^{2/3}$.

3.3. Nanoindentation measurements

The three laser-cracked fused-silica specimens ($N =$ 100, 300 and 500 laser shots) were nanoindented with 10 indents each at different positions relative to the centre of their laser-induced crack, using an applied load of 350 mN, which is 14% above the lower limit of the instrument. (This value was chosen to obtain the most accurate measurement without affecting further tests on the samples, such as fracture in four-point flexure.) An unstressed sample (free of any laser-induced crack) was used to establish the accuracy of the nanoindenter results. This was done by performing 50 nanoindents at different positions across the unstressed fused-silica sample, under the same applied load (350 mN). The mechanical parameters determined from these initial tests were Young's modulus (E) and the hardness (H)

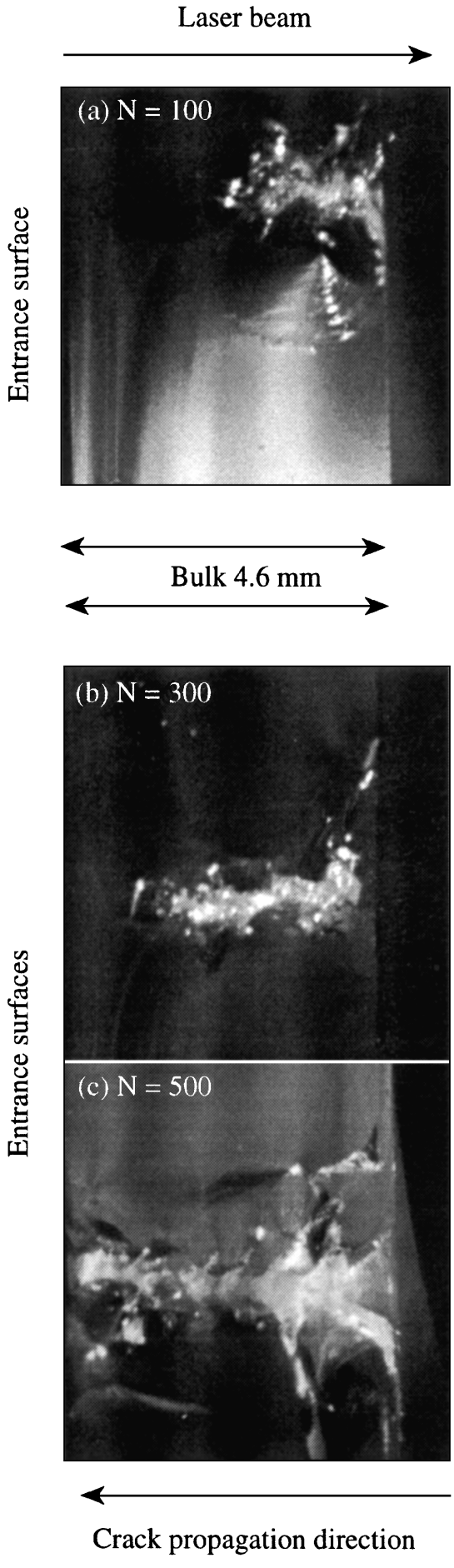

Figure 5 Cross-sectional view of laser-induced cracks produced in fused silica at a laser fluence of $F_L = 2.2 \times F_{exit/th}$ for (a) $N = 100$ laser shots, (b) $N = 300$ laser shots, and (c) $N = 500$ laser shots. The crack depth increases with the number of laser shots.

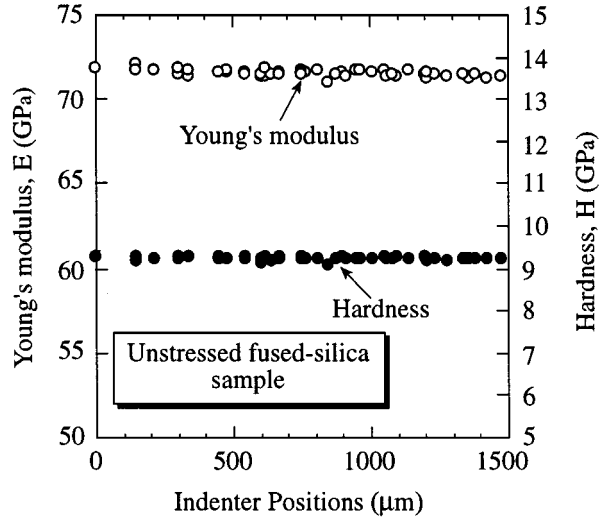

Figure 6 Young's modulus (left vertical scale) and hardness (right vertical scale) versus indenter position (relative to the first indentation) for an unstressed fused-silica (free of any laser-induced cracks) sample obtained under an applied maximum load of 350 mN. The average values are 71.5 GPa for Young's modulus and 9.22 GPa for hardness, which are very close to the literature values ($E = 72$ GPa, $H = 9$ GPa).

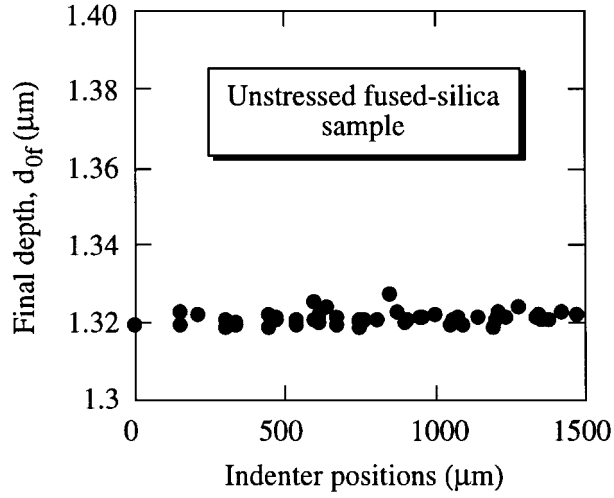

Figure 7 Final penetration depth, d_{0f}, versus indenter position for an unstressed fused-silica sample obtained under conditions of Fig. 6. The depth is almost constant (average value = 1.322 μm) within an error of 0.03 μm.

of fused silica. The statistical results of these tests are quantitatively illustrated in Fig. 6. It is clearly seen that Young's modulus and the hardness obtained are both in very good agreement with the literature-tabulated values of E (72 GPa) [31] and H (9 GPa) [41] for room-temperature fused silica. Furthermore, Fig. 7 shows the measured final penetration depth, d_{0f}, versus the position of the nanoindentations for the same unstressed sample. It is within $\pm$ 3% constant everywhere and can be averaged to $d_{0f} \approx 1.322$ μm.

Next, in Figs 8 and 9 the variations of Young's modulus and hardness for three crack-stressed fused-silica samples are plotted as a function of the distance from the crack center. The measured values for the final penetration depths, d_{f^*}, for the same stressed samples are shown in Table II. It is noted that E^*, H^*, and d_{f^*} are strongly affected by the laser-induced crack dimensions

TABLE II Experimental data from the nanoindentation experiments for the three fused-silica samples used here.

N	x_0 (μm)	y (μm)	r (mm)	d_{f^*} (± 0.03) (μm)	σ_r nanoindenter (MPa)	σ_r inclusion model [16] (MPa)
100	150	0	0.664	1.3252	0.64	0.6
	245	180	0.757	1.3240	0.48	0.5
	290	280	0.829	1.32324	0.15	0.17
	310	280	0.848	1.32304	0.33	0.20
	390	290	0.87	1.3228	0.22	0.24
	220	−180	0.732	1.32433	0.52	0.46
	−310	275	0.846	1.323064	0.25	0.21
	−370	310	0.914	1.3224	0.14	0.15
300	331	−16.4	0.793	1.32351	1.51	1.72
	143	121.5	0.802	1.3242	0.11	0.108
	30	0	0.68	1.3105	−4.87	−4.67
	32.76	90.55	0.689	1.3129	−3.1	−3.5
	55.15	146.72	0.72	1.3174	−1.42	−1.49
	143.18	230.56	0.826	1.3251	0.22	0.23
	−30	−8.4	0.68	1.3059	−5	−4.7
500	164	0	0.664	1.3523	2.33	2.42
	280	280	0.829	1.3242	0.79	0.81
	−360	380	0.94	1.3194	−0.4	−0.36
	−440	450	1.04	1.3185	−0.83	−0.73

x_0 is the position of the indent relative to the border of the laser-induced crack in the x-direction.

$$r = \left[\underbrace{(c + x_0)^2}_{x^2} + y^2 \right]^{1/2}$$

is the position of the indent relative to the center of the laser-induced crack. σ_r is the value of residual stress at the r position of the indent.

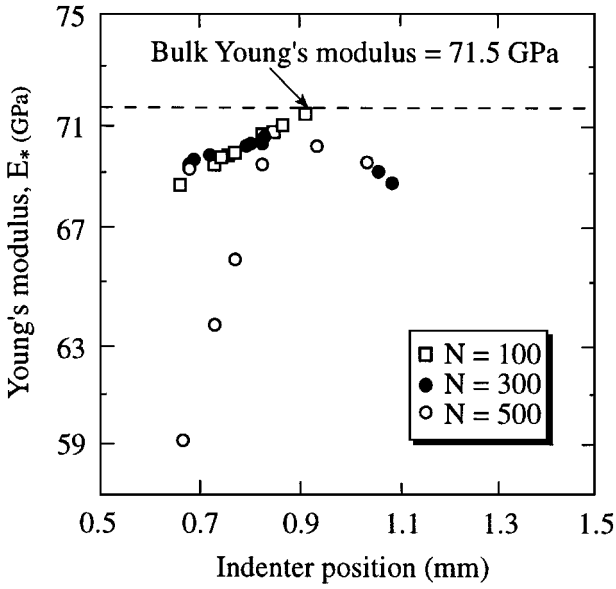

Figure 8 Young's modulus for three crack-stressed, fused-silica samples as a function of distance from the crack center. In general, the Young's modulus from the effect of residual stress from the laser-induced crack deviates further from the bulk value the closer the indent is made to the laser-induced crack. This behaviour is the same for the three samples except at a distance of 0.95 mm from the centre of the crack for samples irradiated with higher number of laser shots ($N = 300$ and 500). Effectively, instead of tending to the bulk value, Young's modulus starts decreasing again as the distance increases. This is probably because of the highest range of the compression stresses resulting from the increase in the crack depth for the corresponding laser-induced cracks. But at further distances, it will tend without any doubt to the bulk value.

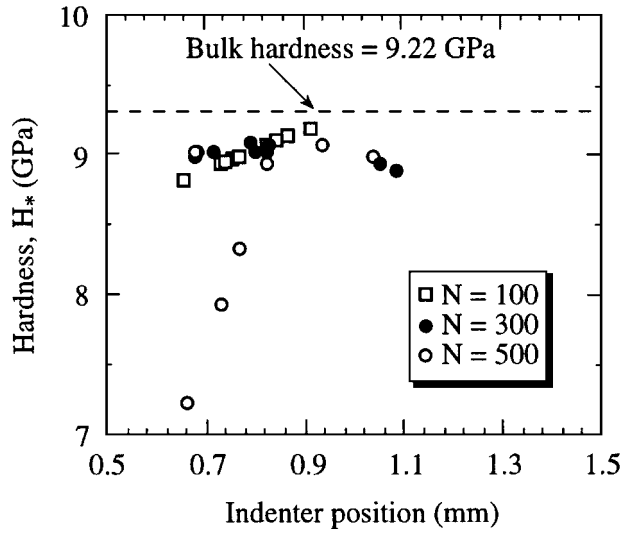

Figure 9 Hardness versus indenter position for three stressed fused-silica samples under conditions similar to Fig. 8.

(predominantly the crack depth), suggesting that the corresponding residual stress field is similarly affected.

Using Equation 6, the residual stress field is calculated for each measurement point around the laser-induced crack ($K_C = 0.75$ MPa $m^{1/2}$), and the corresponding results are plotted in Fig. 10a, b and c versus the nanoindent positions. Fig. 10a, b and c show that the residual stress field in a given direction decreases as the distance of the nanoindents from the centre of

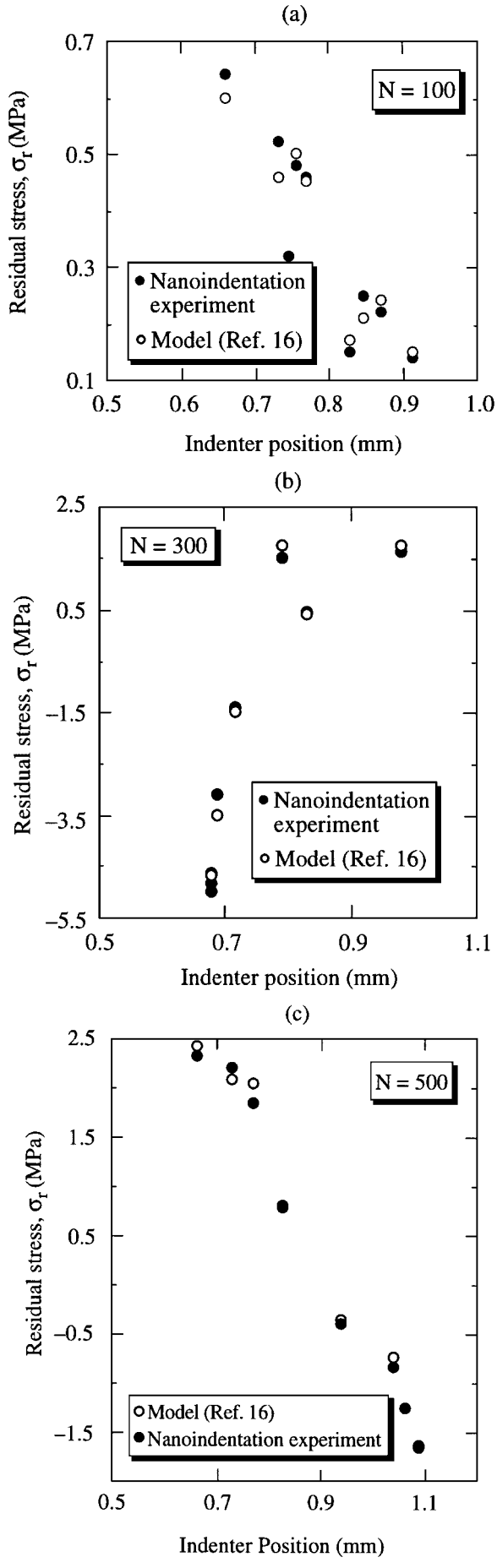

Figure 10 Residual stress as a function of indenter position for three crack-stressed, fused-silica samples: (a) $N = 100$ laser shots, (b) $N = 300$ laser shots, (c) $N = 500$ laser shots. Also reported for comparison are predictions by the inclusion model [16].

the laser-induced crack increases. Contributions by the residual stress field resulting from the polishing process may be added to the stress values in Fig. 10a, b, and c. Effectively, experimental observations [33–37] have established that during the polishing process, upon application of large compressive stresses in the range 3 to 13 GPa, fused silica deforms permanently. The permanent deformation consists primarily of densification [32] and possibly shear deformation. Bridgman and Simon [33] were the first to report such silica densification by showing that the dimensions of specimens of fused silica were permanently changed when subjected to compression. These authors found a threshold pressure of 10 GPa for fused silica, with substantial permanent densification ($\Delta\rho/\rho$) ($\approx 7\%$ at 20 GPa) above this pressure. In subsequent studies by Cohen and Roy [34] the onset of pressure at which densification initiated was about 2 GPa. They also showed that the presence of shear stresses increased the densification. Meade and Jeanloz [35] reported experimental data on the static compression of fused silica. Upon compression by pressures exceeding about 10 to 12 GPa, their samples exhibited irreversible densification under hydrostatic conditions. Upon decompression, the densification was permanent. Yokota *et al.* [36] used the densification of fused silica to explain the observation that during the polishing process a thin surface layer of higher refractive index than that of bulk silica was formed. Densification was thought to occur as a result of the high localized stresses during the polishing process (the index of refraction increased by about 0.2% to 0.4%). In the range of experimental conditions, the depth of the affected layer was found to be 35 to 55 nm. Malin and Vedam [37] also studied the surface layer formed during the polishing of fused silica. They found densified surface layers (20 to 70 nm in thickness) in which the index of refraction was larger by 0.2 to 4.6% as compared to bulk silica. By: (1) assuming a densification of fused silica during the polishing process of the samples used here; (2) setting the onset of pressure at which densification initiates between 3 to 10 GPa; and (3) finally assuming an average densification depth of 50 nm, it follows from the relative wave retardance $\Delta\Gamma = C\sigma t$ ($C = 3.45$ nm $\times$ cm/kgf is the birefringence constant for fused silica, t is the thickness of the sample, σ is the onset pressure for densification) {see Ref. [16]}, that a correction of ± 0.5 nm to ± 2 nm of retardance corresponding to a measured residual stress of ± 0.03 MPa to ± 0.12 MPa {Equation 4 in Ref. [16]} needed to be made.

For comparison, the results of the inclusion model developed by Dahmani *et al.* [16] are also plotted in Fig. 10. The calculated residual stress field from nanoindentation measurements agree well with the model predictions. This model treats the laser-induced crack as an inhomogeneous inclusion within a homogenous matrix. The residual stress field, τ_{xy}, is assumed to have shear nature and equals the sum of two stress fields: (1) the stress field at infinity for a flawless specimen, denoted by σ_{in}, and (2) the stress field at infinity for a void with identical shape under remote applied *pure-shear* stress, denoted by $-\sigma_{\text{in}}$. To draw a

TABLE III Laser-induced crack dimensions obtained after irradiation at laser fluence of $F_L = 2.2 \times F_{exit/th} (F_{exit/th} = 10\,J\,cm^{-2})$ for various laser-pulse numbers N

Sample No.	N	$2c$ (mm)	a (mm)	$\sigma_{r(x=c+0.3\,mm/y=0)}$
1	100	0.98	1.66	0.96
2	300	1.3	3.2	1.6
3	500	1.0	4.3	2.8

a and $2c$ represent the crack depth and the crack surface length, respectively. $\sigma_{r(x=c+0.3\,mm/y=0)}$ represents the measured residual stress at the nearest point to the crack, obtained from birefringence measurements {Ref. [16]}.

comparison with birefringence measurements [16] one of this model's approximations was to assume the hoop stress in the radial crack extension from the damaged site (i. e. at $r = c$), $\sigma_{in} = -3\sigma_{r(x=c+0.3\,mm/y=0)}$, with $\sigma_{r(x=0.3\,mm/y=0)}$ being the nearest *measurable* stress (via birefringence). Details of the model can be found in Ref. [16]. To make a direct comparison with the present study (Equation 6), the theoretical expression for the residual stress field, τ_{xy}, around a laser-induced crack from the model of Ref. [16] is given as follows

$$\tau_{xy} = (-3\sigma_r)\left\{1 - \left[2\left(\frac{xy}{r^2}\right)^2\left(2 + 6\frac{c^4}{r^4} - 4\frac{c^2}{r^2}\right) + \left(\frac{x^2 - y^2}{r^2}\right)^2\left(1 - 3\frac{c^4}{r^4} + 2\frac{c^2}{r^2}\right)\right]\right\} \quad (8)$$

with $r = (x^2 + y^2)^{1/2}$.

Table III lists the laser-induced crack dimensions a and c for the three stressed samples ($N = 100$, 300, and 500 laser shots) obtained from fractography of the broken samples under four-point bending. Table III also lists the residual stress values $\sigma_{r(x=c+0.3\,mm/y=0)}$ inferred from birefringence measurements [16].

Judging by the above-presented data, one finds nanoindentation experiments to be a useful diagnostic for: (1) confirming the nature of the residual stress field about a laser-induced crack; and also for (2) verifying one of the assumptions made in the model of Ref. [16], specifically the choice of $\sigma_{in} = -3\sigma_r$ In the model of Ref. [16], the factor 3 was chosen to afford the smallest possible discrepancy ($\leq 10\%$) between the model's predictions and the experimental birefringence results. Owing to the finite He–Ne probe beam size, the value of the residual stress at the very edge of the crack was impossible to measure in those experiments. In the present experiment, however, because of the very small indentations used, it is possible, for the first time, to probe the residual stress field in the immediate vicinity of the laser-induced crack. An example for this is the indents at $x = 30\ \mu m/y = 0$ and $x = -30\ \mu m/y = -8.4\ \mu m$ for the sample irradiated with $N = 300$ laser shots (see Table II). The residual stress value at these indentation positions was found to be approximately -5 MPa, which is close to $-3\sigma_{r(x=c+0.3\,mm/y=0)}$ for $\sigma_{r(x=0.3\,mm/y=0)} = 1.6$ MPa (deduced from birefringence) for the same sample ($N = 300$).

This close agreement between the model of Ref. [16] and the current nanoindentation experiments underscores the usefulness of the nanoindentation technique for high-spatial-resolution and high-accuracy stress mapping.

4. Conclusion

A new technique using nanoindentation to measure the residual stress field about a laser-induced crack in fused silica is presented. The very small impressions characteristic for this technique allow both very accurate and high spatial-resolution measurements. A simple analysis is used to calculate this residual stress based on the indenter final penetration depth, Young's modulus, and the material hardness at a specific position of the indent relative to the centre of the laser-induced crack. Both Young's modulus and hardness are found to decrease from their respective bulk values with decreasing distance from the crack and approach their respective bulk values far from the crack where the effect of the residual stress becomes negligible.

Measured Young's modulus and hardness values of 71.5 ($\pm$ 0.4) GPa (tabulated value = 72 GPa) and 9.22 ($\pm$ 0.1) GPa (tabulated value = 9 GPa), respectively, from tests on an unstressed fused-silica sample (free of any laser-induced crack) show the high accuracy and high reliability of the nanoindentation diagnostic.

Comparison of measured residual stress field with the predictions of the inclusion model shows good agreement and confirms the shear nature of the residual stress (discussed in the inclusion model) emanating from a laser-induced crack.

Acknowledgements

This work was supported by the US Department of Energy Office of Inertial Confinement Fusion under Cooperative Agreement No. DE-FC03-92SF19460, the University of Rochester, and the New York State Energy Research and Development Authority. The support of DOE does not constitute an endorsement by DOE of the views expressed in this article. One of the authors (F. D.) is thankful to the Laboratory for Laser Energetics for a F. J. Horton Fellowship.

References

1. J. H. CAMPBELL and F. RAINER, in "Damage to space optics and properties and characteristics of optical glass," Vol. 1761, edited by A. J. Marker and J. B. Breckinridge (SPIE, Bellingham, WA, 1993) p. 246.
2. J. H. CAMPBELL, G. J. EDWARDS and J. E. MARION, in First Annual International Conference on Solid State Lasers for Application to Inertial Confinement Fusion, Vol. 2633, edited by M. André and H. T. Powell (SPIE, Bellingham, WA, 1995) p. 522.
3. J. H. CAMPBELL, P. A. HURST, D. D. HEGGINS, W. A. STEELE and S. E. BUMPAS, in "Laser-Induced Damage in Optical Materials: 1996," Vol. 2966, edited by H. E. Bennett, A. H. Guenther, M. R. Kozlowski, B. E. Newnam, and M. J. Soileau (SPIE, Bellingham, WA, 1997) p. 106.
4. M. OHMI, M. AKATSUKA, K. ISHIKAWA, K. NAITO, Y. YONEZAWA, Y. NISHIDA, M. YAMANAKA, Y. IZAWA and S. NAKAI, *Appl. Opt.* **33** (1994) 6368.

5. D. W. FRADIN, *IEEE J. Quantum Electron.* **QE-9** (1973) 954.
6. X. A. SHEN, P. BRAUNLICH, S. C. JONES and P. KELLY, *Phys. Rev. Lett.* **59** (1987) 1605.
7. J. R. MURRAY, J. R. SMITH, R. B. EHRLICH, D. T. KYRAZIS, C. E. THOMPSON, T. L. WEILAND and R. B. WILCOX, *J. Opt. Soc. Am. B* **6** (1989) 2402.
8. N. BLOEMBERGEN, *Appl. Opt.* **12** (1973) 661.
9. R. A. MYERS, N. MUKHERJEE and S. R. J. BRUECK, *Opt. Lett.* **16** (1991) 1732.
10. U. ELLENBERGER, R. WEBER, J. E. BALMER, B. ZYSSET, D. ELLGEHAUSEN and G. J. MIZELL, *Appl. Opt.* **31** (1992) 7563.
11. M. J. SOILEAU and M. BASS, *IEEE J. Quantum Electron.* **QE-16** (1980) 814.
12. N. L. BOLING, M. D. CRISP and G. DUBE, *Appl. Opt.* **12** (1973) 650.
13. Y. Z. LI, M. P. HARMER and Y. T. CHOU, *J. Mater. Res.* **9** (1994) 1780.
14. B. LAWN, "Fracture of brittle solids," Cambridge Solid State Science Series, 2nd ed. (Cambridge University Press, Cambridge, 1993).
15. F. DAHMANI, J. C. LAMBROPOULOS, A. W. SCHMID, S. PAPERNOV and S. J. BURNS, *J. Mater. Res.* (1998), in press.
16. F. DAHMANI, A. W. SCHMID, J. C. LAMBROPOULOS and S. BURNS, *Appl. Opt.* **37**, 1 (1998).
17. P. J. DWIVEDI and D. J. GREEN, *J. Amer. Ceram. Soc.* **78** (1995) 2122.
18. J. B. PETHICA, in "Ion implantation into metals," edited by V. Ashworth, W. A. Grant, and R. P. M. Procter (Pergamon Press, Oxford, 1982) p. 147.
19. D. NEWEY, M. A. WILKINS, and H. M. POLLOCK, *J. Phys. E, Sci. Instrum.* **15** (1982) 119.
20. D. STONE, W. R. LAFONTAINE, P. ALEXOPOULOS, T.-W. WU and C.-Y. LI, *J. Mater. Res.* **3** (1988) 141.
21. K. H. GUENTHER, T. W. HUMPHERYS, J. BALMER, J. R. BETTIS, E. CASPARIS, J. EBERT, M. EICHNER, A. H. GUENTHER, E. KIESEL, R. KUEHNEL, D. MILAM, W. RYSECK, S. C. SEITEL, A. F. STEWART, H. WEBER, H. P. WEBER, G. R. WIRTENSON and R. M. WOOD, *Appl. Opt.* **23** (1984) 3743.
22. Nano Indenter® II, Nano Instruments, Inc., Knoxville, TN.
23. R. K. GOVILA, *Acta Metall.* **20** (1972) 447.
24. N. INGLESTRON and N. NORDBERG, *Eng. Fract. Mech.* **6** (1974) 597.
25. R. R. WILLS, M. G. MENDIRATTA and J. J. PETROVIC, *J. Mater. Sci.* **11** (1976) 1330.
26. J. J. PETROVIC and L. A. JACOBSON, *J. Amer. Ceram. Soc.* **59** (1976) 34.
27. P. CHANTIKUL, G. R. ANSTIS, B. R. LAWN and D. B. MARSHALL, *ibid.* **64** (1981) 539.
28. D. B. MARSHALL and B. R. LAWN, *Commun. Amer. Ceram. Soc.* **No. 1-1** (1981) C-6.
29. D. H. ROACH and A. R. COOPER, *J. Amer. Ceram. Soc.* **68** (1985) 632.
30. G. S. GLAESEMANN, K. JAKUS and J. E. RITTER JR, *ibid.* **70** (1987) 441.
31. W. C. OLIVER and G. M. PHARR, *J. Mater. Res.* **7** (1992) 1564.
32. J. C. LAMBROPOULOS, S. XU and T. FANG, *J. Amer. Ceram. Soc.* **79** (1996) 1441.
33. P. W. BRIDGMAN and I. SIMON, *J. Appl. Phys.* **24** (1953) 405.
34. H. M. COHEN and R. ROY, *Phys. Chem. Glasses* **6** (1965) 149.
35. C. MEADE and R. JEANLOZ, *Phys. Rev. B* **35** (1987) 236.
36. H. YOKOTA, H. SAKATA, M. NISHIBORI and K. KINOSITA, *Surf. Sci.* **16** (1969) 265.
37. M. MALIN and K. VEDAM, *J. Appl. Phys.* **48** (1977) 1155.
38. G. R. ANSTIS, P. CHANTIKUL, B. R. LAWN and D. B. MARSHALL, *J. Amer. Ceram. Soc.* **64** (1981) 533.
39. D. B. MARSHALL and B. R. LAWN, *J. Mater. Sci.* **14** (1979) 2001.
40. D. BROEK, "Elementary engineering fracture mechanics," 3rd rev. ed. (Martinus Nijhoff Publishers, The Hague, The Netherlands, 1982) Chap. 3.
41. J. H. WESTBROOK, *Phys. Chem. Glasses* **1** (1960) 32.

Received 27 June
and accepted 21 July 1998